Report

Adsorption and desorption mechanisms on graphene oxide nanosheets: Kinetics and tuning

Xiaodan Qu,[1,2,4] Qiong Hu,[1] Zhongqian Song,[1] Zhonghui Sun,[1] Baohua Zhang,[1] Jialing Zhong,[1] Xuyou Cao,[1] Yuanjin Liu,[1] Bolin Zhao,[1] Zhenbang Liu,[1,3] Yujie Shen,[1] Yu Bao,[1] Zhenxin Wang,[2,4] Yuwei Zhang,[1,*] and Li Niu[1,3]

*Correspondence: ccywzhang@gzhu.edu.cn (Y.Z.)

Received: January 7, 2021; Accepted: June 15, 2021; Published Online: June 18, 2021; https://doi.org/10.1016/j.xinn.2021.100137

Graphical abstract

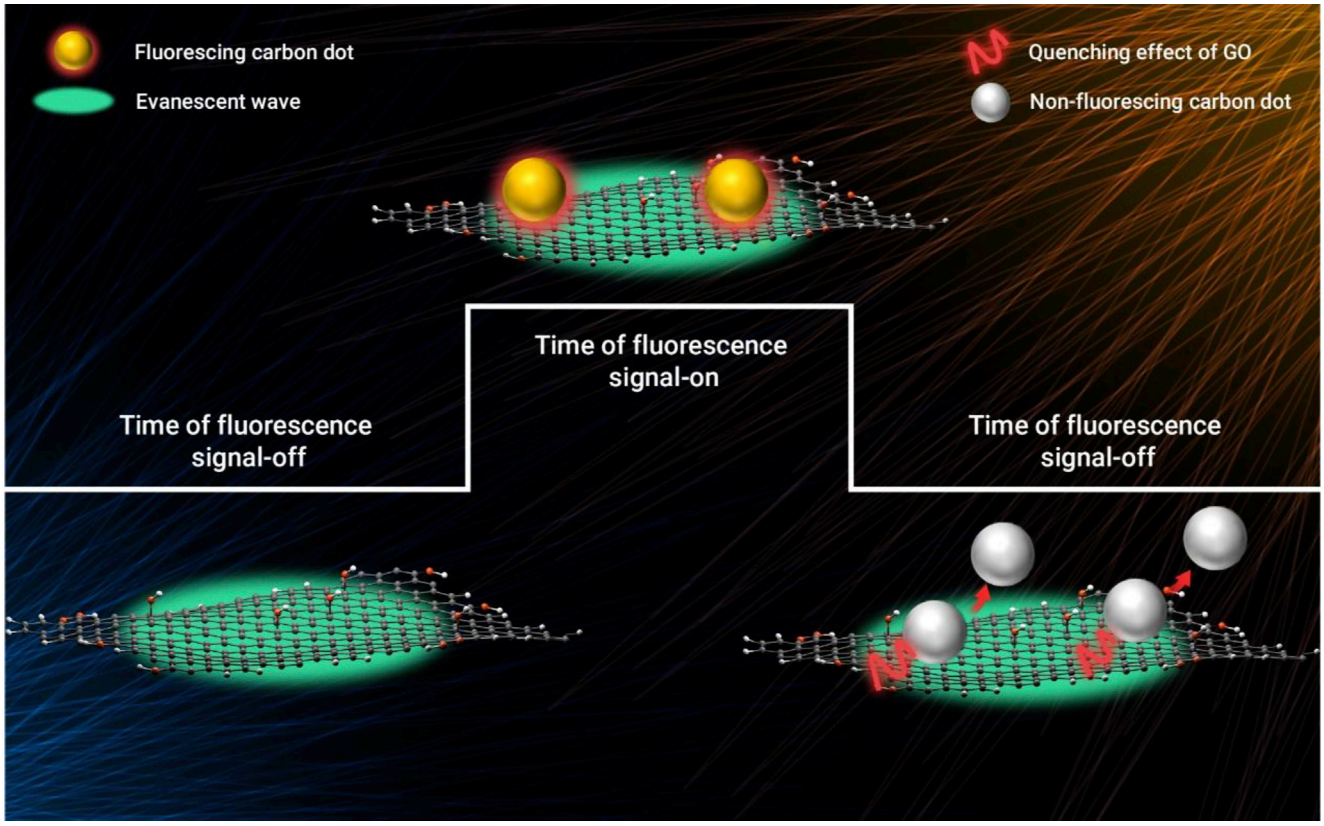

Public summary

- The kinetics of adsorption and desorption process were revealed, respectively, by monitoring a fluorogenic process of carbon dots on the surface of graphene oxides at the single turnover level
- By regulating the equilibrium of adsorption and desorption, a mechanism for the simultaneous promotion of adsorption and desorption has been discovered
- A desorption accelerator could play a satisfactory double action, i.e., adsorption promoter on thermodynamics and desorption promoter on kinetics

Report

Adsorption and desorption mechanisms on graphene oxide nanosheets: Kinetics and tuning

Xiaodan Qu,[1,2,4] Qiong Hu,[1] Zhongqian Song,[1] Zhonghui Sun,[1] Baohua Zhang,[1] Jialing Zhong,[1] Xuyou Cao,[1] Yuanjin Liu,[1] Bolin Zhao,[1] Zhenbang Liu,[1,3] Yujie Shen,[1] Yu Bao,[1] Zhenxin Wang,[2,4] Yuwei Zhang,[1,*] and Li Niu[1,3]

[1]Center for Advanced Analytical Science, c/o School of Chemistry and Chemical Engineering, Guangzhou University, Guangzhou 510006, China

[2]State Key Laboratory of Electroanalytical Chemistry, Changchun Institute of Applied Chemistry, University of Science and Technology of China, Changchun 130022, China

[3]School of Civil Engineering, Guangzhou University, Guangzhou 510006, China

[4]University of Science and Technology of China, Hefei 230026, China

*Correspondence: ccywzhang@gzhu.edu.cn (Y.Z.)

Received: January 7, 2021; Accepted: June 15, 2021; Published Online: June 18, 2021; https://doi.org/10.1016/j.xinn.2021.100137

Citation: Qu X., Hu Q., Song Z., et al., (2021). Adsorption and desorption mechanisms on graphene oxide nanosheets: Kinetics and tuning. The Innovation **2(3)**, 100137.

A knowledge of the adsorption and desorption behavior of sorbates on surface adsorptive site (SAS) is the key to optimizing the chemical reactivity of catalysts. However, direct identification of the chemical reactivity of SASs is still a challenge due to the limitations of characterization techniques. Here, we present a new pathway to determine the kinetics of adsorption/desorption on SASs of graphene oxide (GO) based on total internal reflectance fluorescence microscopy. The switching on and off of the fluorescent signal of SAS lit by carbon dots (CDs) was used to trace the adsorption process and desorption process. We find that sodium pyrophosphate (PPi) could increase the adsorption equilibrium of CDs thermodynamically and promote the substrate-assisted desorption pathway kinetically. At the single turnover level, it was disclosed that the species that can promote desorption may also be an adsorption promoter. Such discovery provides significant guidance for improving the chemical reactivity of the heterogeneous catalyst.

Keywords: adsorption; desorption; fluorescence microscopy; graphene oxide; carbon dots

INTRODUCTION

Adsorption and desorption of reactants have been proved to be the controlling step in a variety of heterogeneous catalysis.[1,2] To improve the activity of catalysts, it is important to accurately obtain the information of the adsorption/desorption process on the surface of a catalyst or catalyst carrier particles.[3–11] However, the main obstacle is, in general, only the overall activity of catalyst or catalyst carrier can be measured, while the adsorption/desorption behavior during the whole catalytic process cannot be distinguished. To date, various techniques have been explored to study the adsorption and desorption processes of surface adsorption sites at atomic resolution, such as *in situ* scanning tunneling microscopy, atomic force microscopy, and *in situ* transmission electron microscopy (TEM).[12–18] Single-molecule spectroscopy was also used to study the weak interaction between dyes and chromatographic columns in chromatography.[19,20] However, information about the kinetics of strong adsorption/desorption processes of catalysis is still lacking.

Currently, total internal reflection fluorescence microscopy (TIRFM) has attracted worldwide interest due to the important role in unraveling the kinetics and dynamics of catalysis at the single-nanoparticle level.[21–26] For instance, TIRFM was used to resolve the active site distribution and the position-related kinetics mechanism of Au nanoparticles.[27] It was also used to study the differences of catalytic kinetics between the plane and edge atoms on shaped Pd nanocrystals.[28,29] However, the application of TIRFM to study the adsorption/desorption kinetics is still challenging. The main obstacle is that it is difficult to distinguish the processes of adsorption and desorption from the reaction process because the reactive probes proved indispensable in previous fluorescent single-molecule kinetics studies. To perform an adsorption/desorption study by TIRFM, a special fluorescent probe, whose fluorescence changes can indicate the adsorption process rather than the chemical reaction process, is highly desired.

In this work, we propose a strategy to perform a TIRFM kinetics study on the adsorption/desorption process, which was realized by selecting one type of fluorescent probe. The off/on fluorescence of such a probe was detected at the single turnover level, which was directly linked with the adsorption/desorption process in sequence. The selected nanomaterial was graphene oxide (GO) nanosheet, in which the surface adsorptive sites of GO play a crucial role when it is used as a catalyst or catalyst carrier in various catalytic reactions and energy conversion processes.[30–34] (The term surface adsorptive site [SAS] denotes a set of special groups of atoms on the surface of GO, usually a defect or flat π network,[35] at which the sorbates adsorbed.) The established fluorescent carbon dots (CDs)[36,37] were used as a prototypical fluorescent probe for *in situ* monitoring the adsorption/desorption process on GO. According to Jiao et al., the fluorescence of CDs can be quenched by adsorbing on GO, which could be recovered by sodium pyrophosphate (PPi), as shown in Figure 1A (Figures S1 and S2).[38] During this quenching process, no chemical reaction occurs between CDs and GO, as confirmed by Fourier transform infrared spectroscopy characterization (Figure S3). Cleavage of chemical bonds is thus excluded between GO and CDs. According to such absorption/desorption studies, absorption models of CDs on SASs of GO nanomaterials were established. To our best knowledge, the absorption/desorption mechanism regulated by electronic effects for GO was disclosed at a single turnover level.

RESULTS

Herein, GO nanosheets were synthesized according to the modified Hummer's method.[39–41] For the TIRFM study on adsorption kinetics on a GO surface, we tentatively selected unique fluorescent CDs as the probe synthesized using the hydrothermal method.[38] The high-resolution TEM (HRTEM) characterization of CDs confirmed their spherical structure and narrow size distribution with an average size of 3.40 ± 0.49 nm (Figure S4). Experimentally, we anchored the diluted GO nanosheets on the surface of the quartz slide in a microfluidic cell, in which fluorescent CDs (with or without PPi) were supplied in a constant flow condition (Figure 1B). The GO on the slide is at the fluorescence-off state when awaiting the adsorption of CDs. When the CDs were introduced into the microfluidic cell, we observed that the surface of the GO nanosheet showed bright spots like stars in the dark light (Figure 1C). Figure 1D displays a portion of representative single turnover fluorescent trajectories from a single spot site shown in Figure 1C. This curve involves multiple burst signals with constant intensity. We performed the following control experiments to ensure the observed fluorescence burst and fluorescence off from adsorption and desorption of CDs. Using CDs as a probe, fluorescence signals were not observed on blank coverslips, ensuring random diffusion of CDs is too weak to be considered as a signal (Figure S7). Fluorescence signals were not observed in the system with only GO with or without PPi (Figure S8). The photobleaching of CDs proved

Report

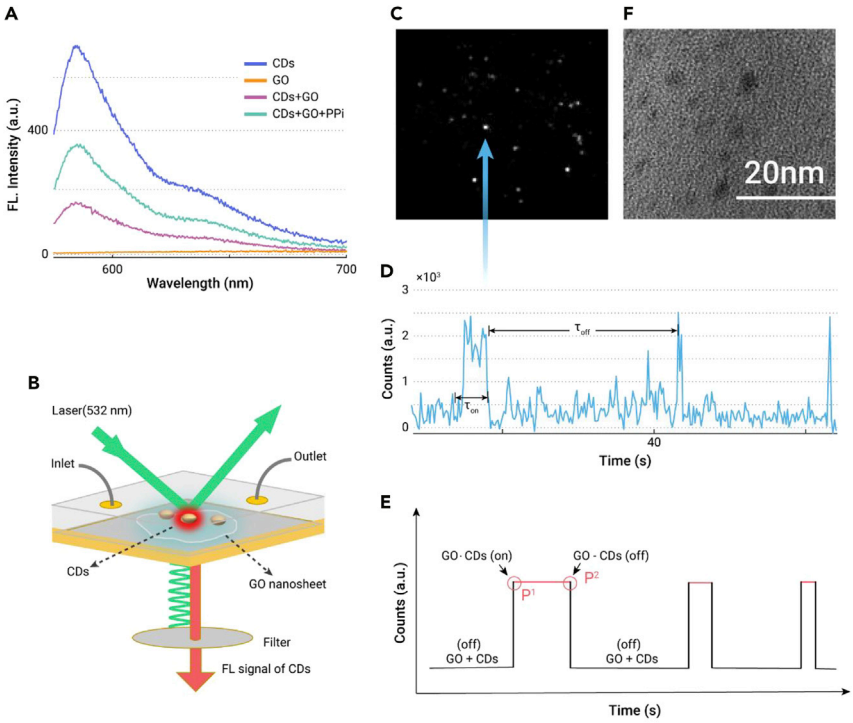

Figure 1. Single adsorption/desorption process detection on a single GO nanosheet (A) Fluorescence spectra of CDs (blue), GO (yellow), a mixture of CDs and GO (purple), and a mixture of CDs and GO with the addition of PPi (green).
(B) Experimental microfluidic quartz cell design using TIRFM for single adsorption/desorption measurement.
(C) A typical optical image for single-dot TIRFM detection.
(D) A typical fluorescence turnover trajectory of the single SAS of GO at an imaging rate of 100 ms per frame.
(E) Schematic illustration of the adsorption/desorption detection principle based on the CDs combined with GO.
(F) TEM image of CDs.

to be very weak in the period of experiments (Figure S9). In Figure 1C, every burst corresponds to an absorption/desorption process, i.e., one time CD adsorption and then desorption turnover from SAS on GO matrix. The corresponding process is described below: as CDs approach the surface of GO (denoted as GO-CDs), SASs are illuminated because the fluorescence of CDs could be excited by the evanescent wave (caused by the total interface reflection of a 532 nm laser). The adsorption state starts as the SASs are illuminated by CDs (p1 point in Figure 1E). As the CDs quench and desorb from SASs, the fluorescence of SASs disappears and a fluorescence-off signal starts (p2 point in Figure 1E). Theoretically, the fluorescence-off signal corresponds to two sub-processes, quenching (denoted as GO-CDs) and desorption. Considering that the quenching process normally occurs instantaneously,[42] we represent this fluorescence-off (τ_{off}) process as the desorption process. When the CDs desorbed from the adsorption site, the SAS of GO was released again. As the next CD was absorbed, the fluorescence-off period finished, and a fluorescence-on period was triggered again. The duration (τ_{on}) of each fluorescence-on signal represents the time waiting for desorption. The averaged fluorescence-on time is represented by $<\tau_{on}>$. The duration (τ_{off}) corresponds to the waiting time for the adsorption of CDs (Figure 1E), while the averaged fluorescence-off time is thus represented by $<\tau_{off}>$. Moreover, statistically, $<\tau_{off}>^{-1}$ and $<\tau_{on}>^{-1}$ represent the time-averaged single adsorption rate and desorption rate, respectively. Resolving the $<\tau_{off}>^{-1}$ and $<\tau_{on}>^{-1}$ enables us to probe the kinetics mechanism of the adsorption and desorption process on the GO in two steps separately.

In this way, the information of adsorption/desorption on GO was obtained by tracing fluorescence-on/off signals of CDs using a signal acquisition system (i.e., EMCCD) of TIRFM. To investigate the effects of the chemical microenvironment on adsorption/desorption, an additional situation was also discussed, in which a substance PPi (promotes fluorescence recovery of CDs, as shown in Figure 1A) was added to the system. In this case, we denote the mixture of CDs and PPi as CDs'. Control experiments confirmed that the observed fluorescent turnover signals came from the absorption/desorption process of CDs on GO. No such distinct fluorescent burst phenomena were observed in the absence of either GO matrix or CDs. It is possible that, after adsorption, some CDs cannot detach from GO. If that happens, no off/on type signals can be observed following the initial off signals. This situation was encountered in our experiment (supplemental information, Figure S7), and we called this "death of SAS." In this article, we took sufficient time (30 min) to rule out these sites at the beginning of the observation, ensuring that the sites detected are active sites.

To study the effect of [CDs] (the concentration of CDs) on the adsorption rate and desorption rate, [PPi] (the concentration of PPi) was set as excess (i.e., 80 mM) so that the effect of [PPi] could be ignored (Figure S1). In the following, we use [S] to represent [CDs] or [CDs']. For the dependence of the concentration of CDs, we observed that, both for CDs and CDs', the adsorption rate saturated with the increase of [S] (Figure 2A). Therefore, the CD concentration dependence on the adsorption rate $<\tau_{off}>^{-1}$ can be described by a one-site Langmuir-Hinshelwood mechanism for adsorption.[21] While the desorption process shows a different [S] dependence, CD and CD' exhibited different behaviors. In the case of [CDs] (Figure 2B), the desorption rate $<\tau_{on}>^{-1}$ of CDs decreased with the increase of [CDs]. This result is reasonable because CDs, as a product, inhibit the desorption of CDs from the surface of GO. This conforms to the characteristics of direct desorption behavior (step iv in Figure 2E). In the case of the dependence of [CDs'] on the desorption process, the rate $<\tau_{on}>^{-1}$ of CDs' was barely influenced by [CDs']. Compared with the situation of [CDs], this may indicate a substrate-assisted desorption pathway in the situation of CDs' because the desorption rate of which could increase with [CDs']. Therefore, the results in Figure 2C could be a result of the interaction of multiple desorption pathways. Accordingly, the total mechanism for the adsorption/desorption process was proposed, which involved one-site absorption and substance-assisted desorption as shown in Figure 2E.[21]

Following a single turnover kinetic analysis,[21] for the one-site adsorption mechanism of CDs, the adsorption rate $<\tau_{off}>^{-1}$ could be expressed as Equation (1).[43]

$$<\tau_{off}>^{-1} = \frac{\gamma_{eff} K_A [S]}{1 + K_A [S]} \qquad \text{(Equation 1)}$$

where γ_{eff} represents the combined reactivity of all possible groups in one SAS on the surface of GO nanosheets. [S] is the concentration of CDs or CDs'; K_A is the adsorption equilibrium constant of CDs or CDs'.

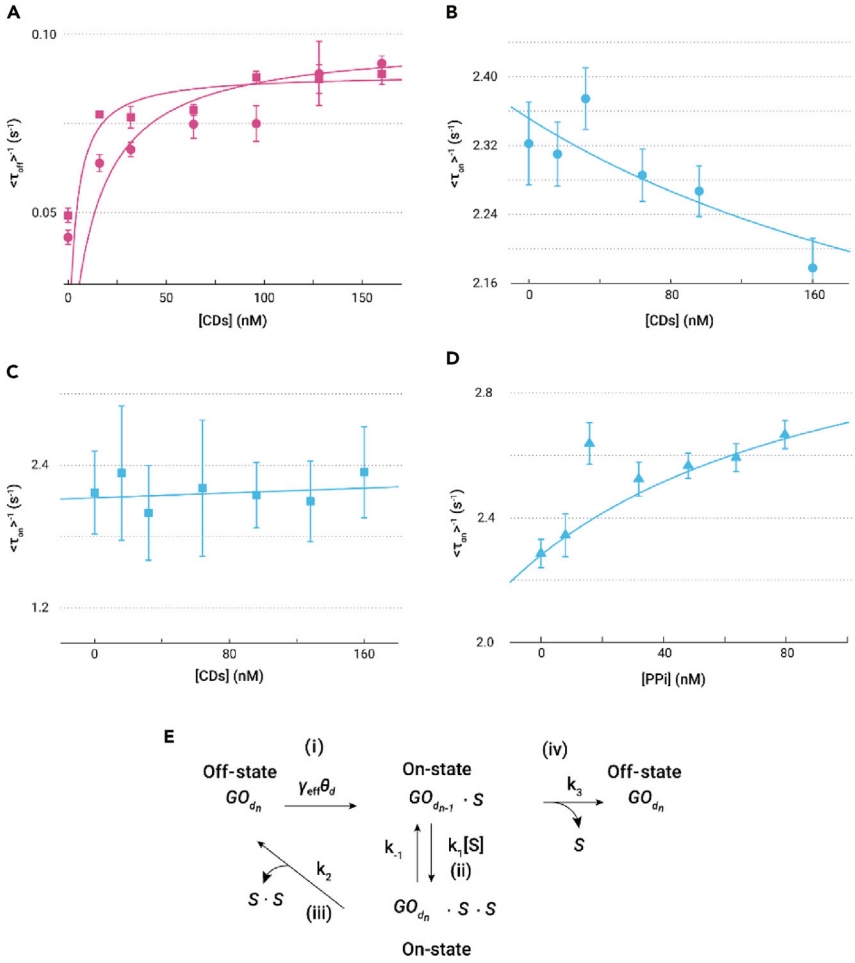

Figure 2. Kinetics study of adsorption and desorption process of CDs on GO (A) CDs concentration dependence of $<\tau_{off}>^{-1}$ with PPi (80 mM, squares) or without PPi (circles). (B) CDs concentration titrations of $<\tau_{on}>^{-1}$ without PPi. (C) CDs concentration titrations of $<\tau_{on}>^{-1}$ with 80 mM PPi. (D) PPi concentration titrations of $<\tau_{on}>^{-1}$ with 32 nM CDs. Each data point in (A–D) is averaged over above 80 turnover trajectories, with the error bar S.E.M. Solid lines in (A–D) are simulations of Equations 1 and 2.
(E) Diagram of the kinetic mechanism for the adsorption/desorption turnover. *d*, SASs on GO; S, CDs or CDs'; n, the number of special groups of atoms in one SAS; γ_{eff}, the effective rate constant for the CDs or CDs' adsorption process; θ_d, the fraction of the surface of SASs occupied by CDs; k_i, the rate constants for different desorption process.

To study the effect of PPi on the adsorption process, the data of CDs and CDs' in Figure 2A were fitted with Equation (1). For the adsorption process, this gives γ_{eff}(CDs) = 0.098 ± 0.004 s^{-1}, which is slightly higher than γ_{eff}(CDs') (0.089 ± 0.003 s^{-1}). Obviously, from the perspective of adsorption kinetics, the adsorption reactivity toward CDs' is lower than that of CDs. In addition to the reactivity γ_{eff} of SASs on GO, we could also obtain the adsorption equilibrium constant of CDs on SASs, which represents the adsorption capacity of SASs. Fitting the data of CDs and CDs' in Figure 2A with Equation (1) gives K_A(CDs) = 0.077 ± 0.079 nM^{-1}, which is much lower than K_A(CDs') = 0.308 ± 0.045 nM^{-1}. It is surprising that, for the CDs' studied here, the lower adsorption reactivity correlated with the stronger binding of CD' to the SASs. A possible reason lies in the fact that the adsorption of CDs' was hindered by the steric hindrance of PPi; this resulted in the lower adsorption reactivity. For the adsorption process, we derived Equation (1a) from Equation (1), which is shown below:

$$<\tau_{off}>^{-1} = \frac{\gamma_{eff}[S]}{\frac{1}{K_A}+[S]} \qquad \text{Equation (1a)}$$

According to Equation (1a), when $[S]\rightarrow 0$, $\frac{1}{K_A}+[S]$ equals $\frac{1}{K_A}$ approximately, then we have

$$<\tau_{off}>^{-1} = K_A\gamma_{eff}[S] \qquad \text{(Equation 1b)}$$

In this condition, $<\tau_{off}>^{-1}$ is determined by γ_{eff} and K_A. Therefore, the addition of PPi increased the adsorption equilibrium constant K_A, resulting in a higher adsorption rate at low [CDs']. As shown in Figure 2A, the adsorption rate of CDs is lower than that of CDs' at low [S], indicating a thermodynamics control adsorption mechanism of CDs.

When $[S]\rightarrow\infty$ approximately equals [S], then we have:

$$<\tau_{off}>^{-1} = \gamma_{eff} \qquad \text{(Equation 1c)}$$

In this condition, the rate of adsorption is determined by the kinetics rate constant γ_{eff} of the adsorption process. At high [S], the adsorption rate of CDs is a little higher than that of CDs', indicating a kinetics control adsorption of CDs. By taking the intersection of the CDs curve and the CDs' curve, the critical transition concentration can be determined as 97.6 nM.

Combining the two cases, it is concluded that the addition of PPi inhibits the adsorption process in kinetics at high [S] and promotes the adsorption in thermodynamics at low [S], and the rate of absorption is co-controlled by kinetics and thermodynamics at medium [S].

Based on the above-mentioned analysis, it can be concluded that the addition of PPi can enhance the strength of the interaction between CDs and GO, but has little effect on the adsorption rate. However, this result cannot explain the fluorescence recovery induced by PPi. Therefore, we further studied the influence of PPi on the desorption process.

The [S] dependence of the desorption rate for a direct desorption pathway and a substrate-assisted product desorption pathway of CDs can be expressed as Equation (2) according to single turnover kinetic analysis.[21] The equation connecting $<\tau_{on}>^{-1}$ with conventional kinetic parameters is[21]:

$$<\tau_{on}>^{-1} = \frac{k_2G_1[S]+k_3}{1+G_1[S]} \qquad \text{(Equation 2)}$$

The parameter definitions in Equation (2) includes: k_2 and k_3 are the rate constants for CD desorption in the substrate-assisted desorption pathway and the direct desorption pathway, respectively; $G_1 = \frac{k_1}{k_{-1}+k_2}$ is a complex

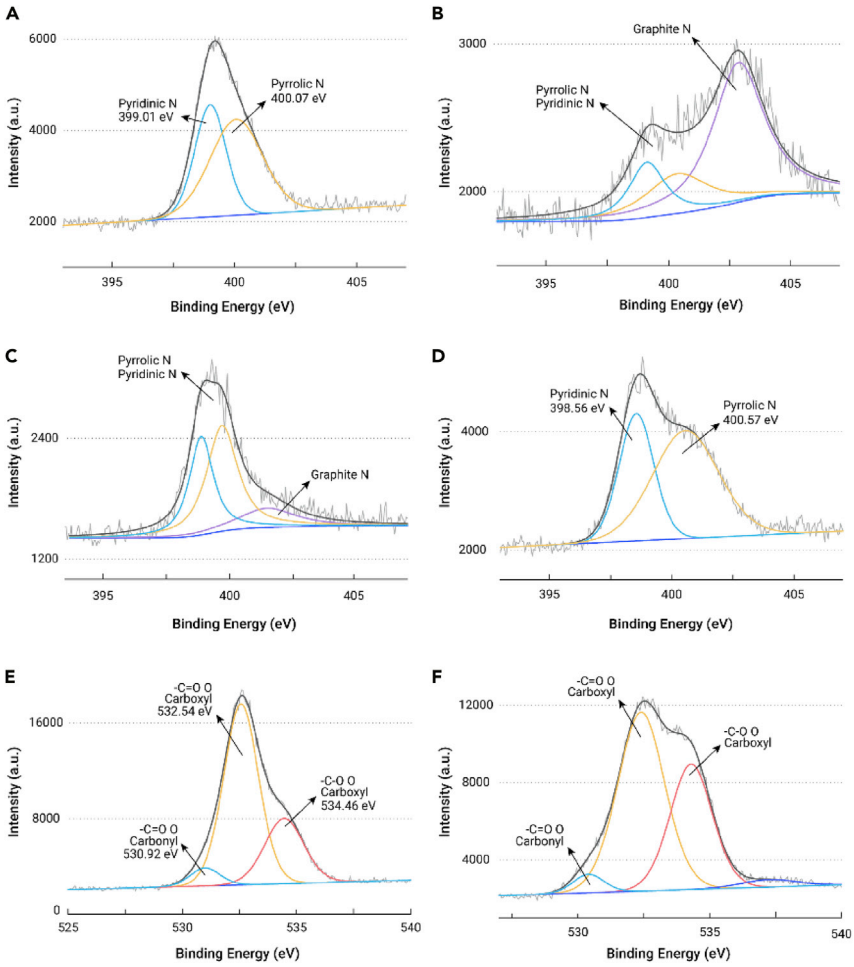

Figure 3. XPS N1s spectra and XPS O1s spectra (A–D) The fitting results of N1s spectra recorded for (A) CDs, (B) CDs + GO, (C) CDs + GO + PPi, and (D) CDs + PPi.
(E and F) The fitting results of O1s spectra were recorded for (E) GO, and (F) GO + PPi.

parameter that is related to both the substrate adsorption and desorption; [S] stands for the [CD] (without PPi) or [CDs'] (with PPi).

The τ_{on} process represents the waiting time for desorption of fluorescent CDs on the GO surface. According to Figure 2E and Equation (2), the product desorption rate could have three types of kinetic behavior in different conditions. (1) When $k_2<k_3$, the $<\tau_{on}>^{-1}$ asymptotic decreases with increasing [CDs]. The direct desorption of CDs falls into this category as shown in Figure 2B, which means CDs on GO prefer the direct desorption pathway when PPi is absent (Figure 2E); (2) $<\tau_{on}>^{-1}$ is in constant at any [CDs] if $k_2 = k_3$ or $G_1 = 0$. Obviously, in the presence of PPi, the direct desorption of CDs coexists with substrate-assisted desorption. To explore the role of PPi in the desorption process, the PPi concentration titration was analyzed. When [CDs] is fixed at 32 nM,$<\tau_{on}>^{-1}$ asymptotically increase with increasing [PPi] (Figure 2D). This kinetic behavior was considered as type (III) in the condition of $k_2>k_3$ in Equation (2), that is the CDs prefer the indirect desorption pathway.

By fitting the sites-averaged $<\tau_{on}>^{-1}$ with Equation (2), the value of k_2, k_3 could be obtained (Table S1). Firstly, for the CD desorption without PPi, the indirect desorption rate constant k_2 (1.900 s^{-1}) is lower than the direct desorption rate constant k_3 (2.352 s^{-1}), indicating that the CD desorption dominantly takes the direct desorption pathway ($k_2 < k_3$). Secondly, in the case of PPi excess, the desorption rate does not change with [CDs'], indicating that the indirect desorption rate k_2 equals k_3 as shown in Equation 2, which is about 2.180 s^{-1}. The increased k_2 indicates the increase of the indirect desorption process. Thirdly, the [PPi]-dependent product desorption rate additionally reveals that the indirect desorption pathway is promoted by PPi. In the case of CDs with excess content, the data of [PPi] dependence on the desorption rates were fitted with Equation (2). The indirect desorption rate constant k_2 increases to 3.100 s^{-1}, and the direct desorption rate constant k_3 decreases to 2.000 s^{-1} (Figure 2D), suggesting the CDs desorption dominantly takes the indirect desorption pathway ($k_2 > k_3$) This result is consistent with the kinetics analysis as shown in Figure 2E. In a word, the incorporation of PPi dominantly changes the desorption pathway of CDs from the direct pathway to the indirect pathway.

DISCUSSION

Accordingly, the fluorescence recovery process of PPi on CDs (shown in Figure 1A) is rationalized as follows: the existence of PPi promotes the adsorption of CDs on GO since adsorption equilibrium constant K_A is increased by adding PPi. In the case of adsorption, PPi plays the role of adsorption accelerator, which is not conducive to the desorption of CDs from the surface of GO. As for the fluorescence recovery of CDs with PPi, it benefits from the PPi-induced indirect desorption of CDs, which is called the substrate-assisted desorption pathway. Surprisingly, PPi not only promotes adsorption but also promotes desorption. This information is of great significance to adjust the balance of adsorption of reactants and desorption of products to improve the chemical reactivity of heterogeneous catalysts or catalyst carriers.

To understand the origin of the different kinetics and thermodynamics of adsorption and desorption of CDs and CDs', X-ray photoelectron spectroscopy (XPS) experiments were further carried out. As for adsorption, we investigated chemical shifts of the binding energies (E_b) of N1s in CDs with and without PPi. It is worth noting that the N sites on CDs are considered as the active sites in the adsorption process according to XPS results: for N1s, it is shown that the N atoms mainly exist in two different chemical states in CDs (Figure 3A), i.e., 399.01 and 400.07 eV, corresponding to pyridinic N

and pyrrolic N, respectively.[44] When CDs are loaded on GO, the content of pyridinic N and pyrrolic N decreases significantly. Meanwhile, a new peak appears at an E_b of 402.80 eV, which is ascribed to the graphite N (Figure 3B). When PPi was added to the mixture, the graphite N is decreased and pyrrolic N and pyridinic N is recovered in content (Figure 3C). This suggests that the element of N should be the adsorption sites of CDs and evolves into graphite N when binding with GO. Therefore, we mainly discussed the chemical shifts of N1s. Compared with N1s in CDs, the N1s of pyridinic N shifted to a lower E_b position and the N1s of pyrrolic N shifted to a higher E_b position in the mixture of CDs and PPi, as shown in Figure 3D. The regulation of E_b is determined by the role of N in the conjugated structure: in the structure of pyridine, the N atom is an electron-withdrawing group, and in the conjugated structure of pyrrole, N is the electron-donating group.[45] Therefore, when a compound with satisfactory electronegativities, such as PPi here, is added to the system, pyridine N further acquires electrons from PPi, resulting in the lowered E_b for the pyridinic N1s as observed. Meanwhile, electron-donating pyrrole N further loses electrons to PPi, which is accompanied by the higher E_b for pyrrolic N1s. These results suggest that PPi plays the role of the electronic regulator to different states of N atoms. The regulation may be responsible for the enhanced adsorption equilibrium constants of CD'.

For the process of desorption, the XPS data of O1s for GO and a mixture of GO and PPi could be used to explain the specific pathway of desorption. As shown in Figure 3E, the peaks at about 530.92, 532.54, and 534.46 eV correspond to carbonyl C=O, carboxyl C=O, and C-O in GO, respectively.[46] Compared with O1s of GO, the O1s peak positions of the mixture of GO and PPi totally move to the lowered E_b at 530.38, 532.37, and 534.28 eV (Figure 3F). This slightly changed E_b indicates the existence of weak electron transfer between PPi and GO. This weak adsorption of PPi on GO may lead to the substrate-assisted desorption of CDs from GO.

Based on the above analysis of XPS spectra, it can be concluded that PPi and CDs have an obvious interaction, which is reflected in the chemical shifts of the E_b of the N1s peak position. In the presence of PPi, the interaction between CDs and GO is enhanced due to the strong interaction between PPi and CDs, which results in much higher K_A values. While, for the desorption process, the XPS spectra of O1s for GO and the mixture of GO and PPi imply a weak interaction between GO and PPi. On the one hand, this weak interaction between PPi and GO could lead to the substrate-assisted desorption pathway, resulting in the overall phenomenon of fluorescence recovery; on the other hand, the existence of PPi also reduces the adsorption rate γ_{eff} due to the steric effect as mentioned earlier.

In summary, adsorption and desorption were regulated here to reveal the kinetics of the adsorption/desorption process on the surface of GO nanosheets. The activity of adsorption sites and the kinetics mechanism of the adsorption/desorption process were revealed at the single turnover level based on TIRFM. Importantly, it was found that the adsorption/desorption process between the sorbate (fluorescent CDs) and GO can be manipulated by an external species, i.e., PPi used herein. Due to the strong electronic effect between PPi and CDs, the equilibrium constant of adsorption was enhanced, resulting in high adsorption activity. The addition of PPi also provided a new substance-assisted desorption pathway for the desorption of CDs. This new desorption pathway resulted in the promoted desorption of CDs from GO and fluorescence recovery of the CDs. In other words, PPi, which is used as a desorption accelerator, plays a satisfactory double action, i.e., adsorption promoter on thermodynamics and desorption promoter on kinetics. It is anticipated that such a new discovery at single turnover level resolution would provide a fundamental instruction toward the controllable synthesis of heterogeneous catalysts with high chemical reactivity by balancing the adsorption of reactants and desorption of products.

MATERIALS AND METHODS

Materials

P-phenylenediamine and PPi were purchased from Aladdin Chemistry (Shanghai, China). Hydrochloric acid (HCl), sulfuric acid, potassium permanganate, potassium dihydrogen phosphate, and dibasic sodium phosphate were purchased from Guangzhou Chemical Reagent Factory. Graphite powder was purchased from Alfa. All chemicals were obtained from commercial sources and used without any further purification. Dialysis bags (MWCO 1,000 and 10,000) were supplied by Yuanye Biotechnology. Double-distilled water was used for the preparation of all the solutions.

Sample preparation

CDs. CDs were synthesized using a hydrothermal method according to previous work.[38] Firstly, the pH of 20 mL of an aqueous solution containing 2 mmol P-phenylenediamine was adjusted to 3.2 by adding HCl. After stirring, the solution was transferred to a poly(tetrafluoroethylene) Teflon-lined autoclave (50 mL) and heated in an oven at 200°C for 8 h. To remove large particles, the obtained purple-red suspensions were centrifuged at 10,000 rpm for 15 min. Then, excess ions and small particles were removed by dialyzing in a cellulose ester membrane (MWCO 1,000) against deionized water for 3 days. The retentate was collected and dried by lyophilization to obtain the powder. Then the powder was dispersed in 0.01 M phosphate buffer solution (pH 7.4) to obtain a solution containing 0.32 mg/mL CDs. In this work, we convert the mass concentration to molarity by the following method.

GO. GO was synthesized by oxidation of graphite according to the modified Hummer's method.[39–41] In brief, 60 mL of the sulfuric acid was placed in a 250 mL beaker, then graphite (2.0 g) was added under stirring. Potassium permanganate (6 g) was slowly added with vigorous stirring while keeping the beaker in an ice bath to ensure the temperature of the suspension was maintained lower than 20°C. Then, the solution was stirred in a thermostatic heating cover for an extended amount of time until the water was almost removed. Water and 1:10 HCl aqueous solution (1 L) were added followed by slow addition of 3 mL of H_2O_2. The color of the solution changed from black to brown and then to yellow. The mixture was washed with dilute hydrochloric acid and centrifugation three times to remove metal ions and the acid. The precipitate was diluted with water and dialyzed for 3–5 days.

Characterization

The pH measurements were performed with a pH-meter FE-28 (METTLER TOLEDO). Fluorescence measurements were carried out using an F-4600 Hitachi spectrometer. HRTEM and TEM images were obtained using a JOEL JEM-2100F TEM/STEM operating at 200 kV. XPS was investigated via an ESCALABMKII X-ray photoelectron spectrometer using a monochromatic Al Kα X-ray source.

TIRFM experiments

The quartz slides with two holes connecting polyethylene tubings and the quartz coverslips, sandwiched with a double-sided tape, were assembled to form a shallow sample chamber with a syringe pump to achieve flow control of substrate solution. Before assembly, 50 μL of GO solution (0.05 mg/mL) was dropped onto the slide and washed with a large amount of water to remove unbound substances after incubation for 40 min. A homebuilt prism-type total TIRFM was used to measure the fluorescence of GO surface with a continuous-wave circularly polarized 532 nm laser beam as excitation light source. A series of videos were collected at different substrate concentrations and analyzed with a home-written IDL program, then the fluorescence intensity time trajectories of individual GO sheets were obtained. To calibrate the drift of stage and the flow cell transition, we use large and bright fluorescent dots as markers to calibrate the relative displacement of the sample. If the mark has drifted, adjust the sample stage carefully to keep the drift at an acceptable level.

REFERENCES

1. RIDEAL, and Eric, K. (1948). Adsorption and heterogeneous catalysis. Nature ***161***, 461–462.
2. Lundqvist, B.I. (1983). Theoretical aspects of adsorption and heterogeneous catalysis. Vacuum ***33***, 639–649.
3. Lehtinen, P.O., Foster, A.S., Ma, Y., et al. (2004). Irradiation-induced magnetism in graphite: a density functional study. Phys. Rev. Lett. ***93***, 187202.
4. Hu, F., Patel, M., Luo, F.X., et al. (2015). Graphene-catalyzed direct Friedel-Crafts alkylation reactions: mechanism, selectivity, and synthetic utility. J. Am. Chem. Soc. ***137***, 14473–14480.
5. Gontard, L.C., Chang, L.Y., Hetherington, C.J.D., et al. (2007). Aberration-corrected imaging of active sites on industrial catalyst nanoparticles. Angew.Chem. Int. Ed. ***46***, 3683–3685.
6. Carlsson, J.M., and Scheffler, M. (2006). Structural, electronic, and chemical properties of nanoporous carbon. Phys. Rev. Lett. ***96***, 046806.
7. Ahmad, M.S., and Nishina, Y. (2020). Graphene-based carbocatalysts for carbon-carbon bond formation. Nanoscale ***12***, 12210–12227.
8. Guo, D.H., Shibuya, R., Akiba, C., et al. (2016). Active sites of nitrogen-doped carbon materials for oxygen reduction reaction clarified using model catalysts. Science ***351***, 361–365.
9. Xiang, Q., Yu, J., and Jaroniec, M. (2012). Synergetic effect of MoS_2 and graphene as cocatalysts for enhanced photocatalytic H_2 production activity of TiO_2 nanoparticles. J. Am. Chem. Soc. ***134***, 6575–6578.

10. Wang, X.L., Hou, Z.F., Ikeda, T., et al. (2011). Selective nitrogen doping in graphene: enhanced catalytic activity for the oxygen reduction reaction. Phys. Rev. B. ***84***, 245434.
11. Scheuermann, G.M., Rumi, L., Steurer, P., et al. (2009). Palladium nanoparticles on graphite oxide and its functionalized graphene derivatives as highly active catalysts for the Suzuki-Miyaura coupling reaction. J. Am. Chem. Soc. ***131***, 8262–8270.
12. Hou, Z.F., Wang, X.L., Ikeda, T., et al. (2012). Interplay between nitrogen dopants and native point defects in graphene. Phys. Rev. B. ***85***, 165439.
13. Park, J.W., and Shumaker-Parry, J.S. (2014). Structural study of citrate layers on gold nanoparticles: role of intermolecular interactions in stabilizing nanoparticles. J. Am. Chem. Soc. ***136***, 1907–1921.
14. Engelbrekt, C., Nazmutdinov, R.R., Zinkicheva, T.T., et al. (2019). Chemistry of cysteine assembly on Au(100): electrochemistry, in situ STM and molecular modeling. Nanoscale ***11***, 17235–17251.
15. Gonzalez-Herrero, H., Gomez-Rodriguez, J.M., Mallet, P., et al. (2016). Atomic-scale control of graphene magnetism by using hydrogen atoms. Science ***352***, 437–441.
16. Endo, O., Nakamura, M., Amemiya, K., et al. (2017). Compression-induced conformation and orientation changes in an n-alkane monolayer on a Au(111) surface. Langmuir ***33***, 3934–3940.
17. Li, L., Zhang, R., Vinson, J., et al. (2018). Imaging catalytic activation of CO_2 on Cu_2O (110): a first-principles study. Chem. Mater. ***30***, 1912–1923.
18. Kaiser, K., Gross, L., and Schulz, F. (2019). A single-molecule chemical reaction studied by high-resolution atomic force microscopy and scanning tunneling microscopy induced light emission. ACS nano ***13***, 6947–6954.
19. Wirth, M.J., and Swinton, D.J. (2001). Single-molecule study of an adsorbed oligonucleotide undergoing both lateral diffusion and strong adsorption. J. Phys. Chem. B. ***105***, 1472–1477.
20. Wirth, M.J., Swinton, D.J., and Ludes, M.D. (2003). Adsorption and diffusion of single molecules at chromatographic interfaces. J. Phys. Chem. B. ***107***, 6258–6268.
21. Xu, W.L., Kong, J.S., Yeh, Y.T.E., et al. (2008). Single-molecule nanocatalysis reveals heterogeneous reaction pathways and catalytic dynamics. Nat. Mater. ***7***, 992–996.
22. Zhou, X., Andoy, N.M., Liu, G., et al. (2012). Quantitative super-resolution imaging uncovers reactivity patterns on single nanocatalysts. Nat. Nanotechnol. ***7***, 237–241.
23. Sambur, J.B., Chen, T.Y., Choudhary, E., et al. (2016). Sub-particle reaction and photocurrent mapping to optimize catalyst-modified photoanodes. Nature ***530***, 77–80.
24. Zhang, Y.W., Lucas, J.M., Song, P., et al. (2015). Superresolution fluorescence mapping of single-nanoparticle catalysts reveals spatiotemporal variations in surface reactivity. Proc. Natl. Acad. Sci. U. S. A. ***112***, 8959–8964.
25. Zhang, Y.W., Chen, T., Alia, S., et al. (2016). Single-molecule nanocatalysis shows in-situ deactivation of Pt/C electrocatalysts during the hydrogen-oxidation reaction. Angew.Chem. Int. Ed. ***55***, 3086–3090.
26. Zhang, Y.W., Song, P., Chen, T., et al. (2018). Unique size-dependent nanocatalysis revealed at the single atomically precise gold cluster level. Proc. Natl. Acad. Sci. U. S. A. ***115***, 10588–10593.
27. Zhou, X.C., Andoy, N.M., Liu, G.K., et al. (2012). Quantitative super-resolution imaging uncovers reactivity patterns on single nanocatalysts. Nat. Nanotechnol. ***7***, 237–241.
28. Liu, X.D., Chen, T., Song, P., et al. (2018). Single-molecule nanocatalysis of Pt nanoparticles. J. Phys. Chem. C. ***122***, 1746–1752.
29. Chen, T., Chen, S., Zhang, Y.W., et al. (2016). Catalytic kinetics of different types of surface atoms on shaped Pd nanocrystals. Angew.Chem. Int. Ed. ***55***, 1839–1843.
30. Meng, A.Y., Zhang, L.Y., Cheng, B., et al. (2019). Dual cocatalysts in TiO_2 photocatalysis. Adv. Mater. ***31***, 1807660.
31. Yan, H., Cheng, H., Yi, H., et al. (2015). Single-atom Pd1/graphene catalyst achieved by atomic layer deposition: remarkable performance in selective hydrogenation of 1,3-butadiene. J. Am. Chem. Soc. ***137***, 10484–10487.
32. Lei, C.J., Wang, Y., Hou, Y., et al. (2019). Efficient alkaline hydrogen evolution on atomically dispersed Ni-N_x species anchored porous carbon with embedded Ni nanoparticles by accelerating water dissociation kinetics. Energ. Environ. Sci. ***12***, 149–156.
33. Han, L.L., Liu, X.J., Chen, J.P., et al. (2019). Atomically dispersed molybdenum catalysts for efficient ambient nitrogen fixation. Angew.Chem. Int. Ed. ***58***, 2321–2325.
34. Wei, H.H., Huang, K., Wang, D., et al. (2017). Iced photochemical reduction to synthesize atomically dispersed metals by suppressing nanocrystal growth. Nat. Commun. ***8***, 1490.
35. Chen, X.X., and Chen, B.L. (2015). Macroscopic and spectroscopic investigations of the adsorption of nitroaromatic compounds on graphene oxide, reduced graphene oxide, and graphene nanosheets. Environ. Sci. Technol. ***49***, 6181–6189.
36. Lee, J., Park, I.S., Jung, E., et al. (2014). Direct, sequence-specific detection of dsDNA based on peptide nucleic acid and graphene oxide without requiring denaturation. Biosens. Bioelectron. ***62***, 140–144.
37. Dong, H.F., Gao, W.C., Yan, F., et al. (2010). Fluorescence resonance energy transfer between quantum dots and graphene oxide for sensing biomolecules. Anal. Chem. ***82***, 5511–5517.
38. Jiao, Y., Gong, X., Han, H., et al. (2018). Facile synthesis of orange fluorescence carbon dots with excitation independent emission for pH sensing and cellular imaging. Anal. Chim. Acta ***1042***, 125–132.
39. Hummers, W.S., and Offeman, R.E. (1958). Preparation of graphitic oxide. J. Am. Chem. Soc. ***80***, 1339.
40. Xu, Y.X., Zhao, L., Bai, H., et al. (2009). Chemically converted graphene induced molecular flattening of 5,10,15,20-tetrakis(1-methyl-4-pyridinio)porphyrin and its application for optical detection of cadmium(II) ions. J. Am. Chem. Soc. ***131***, 13490–13497.
41. Xu, Y.X., Lin, Z.Y., Huang, X.Q., et al. (2013). Flexible solid-state supercapacitors based on three-dimensional graphene hydrogel films. ACS Nano ***7***, 4042–4049.
42. Gelinas, S., Rao, A., Kumar, A., et al. (2014). Ultrafast long-range charge separation in organic semiconductor photovoltaic diodes. Science ***343***, 512–516.
43. Xu, W., Kong, J.S., Yeh, Y.T.E., et al. (2009). Single-molecule nanocatalysis reveals heterogeneous reaction pathways and catalytic dynamics. Nano Res. ***2***, 911–922.
44. Song, P., Zhang, Y.W., Pan, J., et al. (2015). Cheap carbon black-based high-performance electrocatalysts for oxygen reduction reaction. Chem. Commun. ***51***, 1972–1975.
45. Choi, H.C., Park, J., and Kim, B. (2005). Distribution and structure of N atoms in multiwalled carbon nanotubes using variable-energy X-ray photoelectron spectroscopy. J. Phys. Chem. A. ***109***, 4333–4340.
46. Stobinski, L., Lesiak, B., Malolepszy, A., et al. (2014). Graphene oxide and reduced graphene oxide studied by the XRD, TEM and electron spectroscopy methods. J. Electron. Spectrosc. ***195***, 145–154.

ACKNOWLEDGMENTS

This work was funded by the Research & Development Projects in Key Areas of Guangdong Province, China (2019B010933001), the National Natural Science Foundation of China (21974033, 21904026), the National Basic Research Program of China (973 Program, 2017YFE0197900), and the Innovation Training Program for College Students of Guangzhou University (CX2019185).

AUTHOR CONTRIBUTIONS

X.Q., Y.Z., Q.H., and L.N. contributed to the conception of the study. X.Q. and Y.Z. performed the experiment. X.Q., Y.Z., and L.N. contributed significantly to analysis and manuscript preparation. X.Q. and Y.Z. performed the data analyses and wrote the manuscript. Z. Song, Z. Sun, B. Zhang, J.Z., X.C., Y.L., B. Zhao, Z.L., Y.S., Y.B., and Z.W. helped to perform the analysis with constructive discussions.

DECLARATION OF INTERESTS

The authors declare no competing interests.

SUPPLEMENTAL INFORMATION

Supplemental information can be found online at https://doi.org/10.1016/j.xinn.2021.100137.

LEAD CONTACT WEBSITE

http://hhu.gzhu.edu.cn/info/1125/2159.htm.